Nano Research Energy

ISSN 2791-0091 (print); 2790-8119 (online)
https://doi.org/10.26599/NRE.2023.9120049

Research Article

High sulfur loading and shuttle inhibition of advanced sulfur cathode enabled by graphene network skin and N, P, F-doped mesoporous carbon interfaces for ultra-stable lithium sulfur battery

Haotian Liu[1,2], Fan Liu[1], Zehua Qu[3], Jieling Chen[1], Hui Liu[1], Yiqing Tan[1], Jiabao Guo[1], Yan Yan[1,3] (✉), Shuang Zhao[1], Xinsheng Zhao[4], Xinming Nie[4] (✉), Xin Ma[5] (✉), Zengxia Pei[6], and Mingkai Liu[1,3] (✉)

[1] *School of Chemistry & Materials Science, Jiangsu Key Laboratory of Green Synthetic Chemistry for Functional Materials, Jiangsu Normal University, Xuzhou 221116, China*
[2] *School of Physics and Astronomy, Sun Yat-sen University, Zhuhai 519082, China*
[3] *State Key Laboratory of Molecular Engineering of Polymers, Department of Macromolecular Science, Fudan University, Shanghai 200433, China*
[4] *School of Physics and Electronic Engineering, Jiangsu Normal University, Xuzhou 221116, China*
[5] *School of Chemistry and Materials Science, Nanjing University of Information Science and Technology, Nanjing 210044, China*
[6] *School of Chemical and Biomolecular Engineering, The University of Sydney, Sydney, New South Wales 2006, Australia*

Received: 18 October 2022 / **Revised:** 28 November 2022 / **Accepted:** 11 December 2022

ABSTRACT

Achieving high loading of active sulfur yet rational regulating the shuttle effect of lithium polysulfide (LiPS) is of great significance in pursuit of high-performance lithium-sulfur (Li-S) battery. Herein, we develop a free-standing graphene-nitrogen (N), phosphorus (P) and fluorine (F) co-doped mesoporous carbon-sulfur (G-NPFMC-S) film, which was used as a binder-free cathode in Li-S battery. The developed mesoporous carbon (MC) achieved a high specific surface area of 921 $m^2 \cdot g^{-1}$ with a uniform pore size distribution of 15 nm. The inserted graphene network inside G-NPFMC-S cathode can effectively improve its electrical conductivity and simultaneously restrict the shuttle of LiPS. A high sulfur loading of 86% was achieved due to the excellent porous structures of graphene-NPFMC (G-NPFMC) composite. When implemented as a freestanding cathode in Li-S battery, this G-NPFMC-S achieved a high specific capacity (1,356 $mAh \cdot g^{-1}$), favorable rate capability, and long-term cycling stability up to 500 cycles with a minimum capacity fading rate of 0.025% per cycle, outperforming the corresponding performances of NPFMC-sulfur (NPFMC-S) and MC-sulfur (MC-S). These promising results can be ascribed to the featured structures that formed inside G-NPFMC-S film, as that highly porous NPFMC can provide sufficient storage space for the loading of sulfur, while, the N,P,F-doped carbonic interface and the inserted graphene network help hinder the shuttle of LiPS via chemical adsorption and physical barrier effect. This proposed unique structure can provide a bright prospect in that high mass loading of active sulfur and restriction the shuttle of LiPS can be simultaneously achieved for Li-S battery.

KEYWORDS

lithium sulfur battery, high sulfur loading, shuttle inhibition, heteroatoms doped interface, graphene network barrier

1 Introduction

With the growing demands for both high energy and power densities of energy devices, lithium-sulfur (Li-S) battery has been considered one of the promising candidates for the next generation batteries due to its ultrahigh theoretical energy density (2,600 $Wh \cdot kg^{-1}$) and specific capacity (1,675 $mAh \cdot g^{-1}$) [1–5]. Different from the insertion reactions in commercial lithium-ion batteries, sulfur can achieve this high theoretical capacity via a distinct conversion reaction. However, the practical application of Li-S battery is hindered by several technical challenges [6, 7]. In detail, (i) the severe dissolution of lithium polysulfide (LiPS) into the electrolyte and their diffusion to the anode side, can cause rapid capacity fading and result in low Coulombic efficiency [8–10]; (ii) the insulating nature of reactive sulfur and its discharged intermediates of Li_2S/Li_2S_2 prevent the rapid electron transportation and further cause the low utilization of active substances [11–13]; (iii) the large

Address correspondence to Yan Yan, yanyan@jsnu.edu.cn; Xinming Nie, nxinming@jsnu.edu.cn; Xin Ma, xmanager12356a@163.com; Mingkai Liu, liumingkai@jsnu.edu.cn

volumetric expansion (~ 80%) of sulfur leads to the destruction of the cathode [14, 15].

Up to now, many strategies have been proposed to resolve the above issues, including (1) developing highly porous substrate to effectively enhance the mass loading of active sulfur [16, 17]; (2) taking polar nanomaterials as sulfur hosts to restrict the shuttle diffusion of LiPS via chemical binding effect [18–20]; (3) constructing porous network or narrow channels to wrap the active sulfur intermediates according to the physical barrier and provide expansion space for the activation of sulfur [21, 22]. These approaches can overcome the existing problems of Li-S battery to a certain extent. Nevertheless, high mass loading of sulfur and the restriction of the shuttle effect for LiPS is a paradox that it is still a big challenge to realize the high mass loading and shuttle restriction simultaneously [23–26]. Ideally, if the support can concurrently achieve the following advantages, such as intrinsically possessing excellent porous structures with large specific surface area, having rich polar interfaces, restricting the shuttle of LiPS by forming physical networks and can integrally form free-standing sulfur cathode without utilization of binder and conductive agents, the conversion of active sulfur will be explicitly intensified and making electrochemical utilization of sulfur/LiPS prominent in the battery chemistry.

Herein, a flexible graphene-nitrogen (N), phosphorus (P), fluorine (F)-doped mesoporous carbon-sulfur (G-NPFMC-S) film is designed as a binder-free cathode for simultaneously enhancing the sulfur utilization efficiency and the stability of assembled Li-S battery. Mesoporous carbon (MC) matrix with a high specific surface area of 921 $m^2 \cdot g^{-1}$ can act as an effective supporting substrate to ensure the high loading of active sulfur, and further provide sufficient space for the expansion of sulfur during the electrochemical charge/discharge processes. N, P, F-doped carbonic interfaces provide a great number of polar sites for the strong chemisorption of LiPS for suppressing the shuttle effect. Meanwhile, graphene sheets inserted inside the G-NPFMC-S film can form a connected network for further restricting the shuttle effect via physical blocking. Meriting by these structural features, G-NPFMC-S achieves an ultrahigh specific capacity of 1,356 $mAh \cdot g^{-1}$, a favorable rate capability, high Coulombic efficiency and long-term cycling stability up to 500 cycles with a minimum capacity fading rate of 0.025% per cycle. These results outperform the electrochemical performances of NPFMC-sulfur (NPFMC-S) and MC-sulfur (MC-S) cathodes, demonstrating the structural features that realized inside G-NPFMC-S film.

2 Experimental

2.1 Materials

Natural graphite platelets (~ 325 mesh particle size) were purchased from Sigma Aldrich. Silicon (IV) oxides (SiO_2) sols (40% in H_2O) with size of 14 nm were obtained from Alfa Aesar. Sucrose, ammonium hydroxide ($NH_4 \cdot OH$, 25%), hydrofluoric acid (HF, ≥ 40.0%), ammonium hexafluorophosphate (NH_4PF_6), sulfur bulk were obtained from Sinopharm Chemical Reagent Co., Ltd. All the chemicals were directly used without further treatment.

2.2 Preparation of water-soluble graphene sheets

Graphene oxide (GO) (Fig. S1 in the Electronic Supplementary Material (ESM)) was synthesized according to a modified Hummers' method [27, 28]. And water-soluble graphene sheets were prepared according to the following steps: GO aqueous dispersion with a concentration of 0.5 $mg \cdot mL^{-1}$ was kept in a flask at 60 °C in an oil bath, and a certain amount of $N_2H_4 \cdot H_2O$ (85%) was added into GO solution with a mass ratio of $N_2H_4 \cdot H_2O$ to GO is about 15:1. The reaction solution was kept at 60 °C for 30 min, and the product was naturally cooled and washed with deionized (DI) water for five times to get a homogeneously dispersed water-soluble graphene sheets dispersion.

2.3 Preparation of MC, NPFMC

Ammonium hydroxide (70 mL) was mixed with sucrose (5 g) under strong stirring and sonication. And then 30 mL of SiO_2 sols were added in the solution. The mixture was poured into a stainless steel autoclave, and the reaction was maintained at 160 °C for 24 h. After being cooled down, the product was dried under vacuum for 12 h. The obtained clay yellow powder was carbonized in Argon at 800 °C for 2 h with a ramping rate of 5 $°C \cdot min^{-1}$. The obtained black materials were treated with hydrofluoric acid (50 mL) at room temperature for 3 h, and the obtained mixture was washed with DI water for five times, in order to realize the preparation of MC nanomaterial.

For the preparation of NPFMC, 200 mg of NH_4PF_6 was mixed with the clay yellow powder in 300 mL DI water, and the mixture was dried at 80 °C under vacuum for 12 h. Then, the obtained powders were treated with high-temperature carbonization at 800 °C for 2 h and were chemically etched by HF (100 mL) for 3 h, finally resulting in the formation of NPFMC.

2.4 Preparation of MC-S, NPFMC-S, G-NPFMC-S

MC-S nanomaterial was synthesized according to a melt-diffusion approach. In detail, MC powder was firstly mixed with native sulfur with a mass ratio of 1:10, which were sealed in a Teflon pot saturated with argon and heated at 170 °C for 24 h. After being cooled down naturally, MC-S nanomaterial can be obtained. NPFMC-S nanomaterial was prepared with the same procedure as that of MC-S with NPFMC substituting MC in the preparation process. For the preparation of G-NPFMC-S, the obtained NPFMC-S (50 g) was dispersed with water-soluble graphene sheets (5 mL, 0.5 $g \cdot mL^{-1}$) under strong stirring and sonication. The mixture was further filtrated under vacuum, finally achieving the preparation of free-standing G-NPFMC-S film.

2.5 Characterizations

The structures and morphologies of prepared samples were characterized by field-emission scanning electron microscopy (SEM, SU-8010, Hitachi). Energy dispersive spectroscopy (EDS) mappings were conducted based on an EDAX analysis system (TEAM Octane Super). X-ray photoelectron spectroscopy (XPS) was performed on a Thermo Fisher Scientific, K-Alpha equipment. The specific surface area and pore size distribution of the products were analyzed by Brunauer-Emmett-Teller (BET, Quantachrome U.S., Autosorb-IQ2-VP). Thermogravimetric analysis was carried out on a TA 50 equipment with a heating rate of 10 $°C \cdot min^{-1}$ in N_2 up to 800 °C. Powder X-ray diffraction (XRD) was performed on Bruker/D8 Advanced with Cu Kα radiation.

2.6 Electrochemical measurements

For assembling Li-S battery, G-NPFMC-S film with a diameter of 13 mm was directly used as the working cathode. A polypropylene (PP) membrane (Cellgard 2400) was utilized as the separator, and fresh lithium foil was used as the anode. Columnar batteries were assembled in a glove box filled in Ar with H_2O and O_2 contents less than 0.1 PPM. 1 M lithium bis(trifluoromethane) sulfonamide (LiTFSI) in 1,3-dioxolane/dimethoxymethane (DOL/DME, 1:1 by volume) with 0.3 M $LiNO_3$ was used as the electrolyte. 40 μL of electrolyte was input in each battery. For MC-S and NPFMC-S electrodes, the MC-S or NPFMC-S (80 wt.%) were mixed with conductive carbon black (10 wt.%), and poly(vinylidene fluoride) binder (10 wt.%) in N-methyl-2-pyrrolidone solvent. The slurry was then cast onto an aluminum foil, dried at 60 °C for 12 h in a vacuum oven for the preparation of MC-S and NPFMC-S cathodes.

Galvanostatic discharge-charge curves at different current were tested in a voltage range of 1.8−2.8 V using a battery test system (Wuhan LAND, CT2100A, China). Cyclic voltammetry (CV) with a scan rate of 0.1 $mV \cdot s^{-1}$ between 1.8−3.0 V were performed on an ARBIN electrochemistry workstation (MSTAT-5V/5mA, 32 channels). Electrochemical impedance spectroscopy (EIS) was performed on a Salartron-Princeton electrochemical workstation from 100 kHz to 0.01 kHz with an applied voltage amplitude of 10 mV. Fresh batteries were used for the EIS test at the open-circuit potential. The specific capacities were calculated based on the mass of sulfur.

3 Results and discussion

Figure 1 schematically illustrates the preparation of G-NPFMC-S film. Firstly, NPFMC was developed based on the precursors of sucrose amine, ammonium hexafluorophosphate and SiO_2 nanoparticles, and was further used as sulfur host substrate for fabricating sulfur containing cathode. Inserting sulfur into NPFMC was realized based on an irrigation strategy, resulting in the preparation of NPFMC-sulfur composite (NPFMC-S). The formed NPFMC-S composite nanoparticles were co-dispersed with graphene sheets (Fig. S2 in the ESM) under strong sonication and stirring. The mixture of graphene and NPFMC-S nanoparticles were treated by vacuum filtration, and finally formed a free-standing G-NPFMC-S film with excellent porous architecture and high sulfur loading (86%). These structural features will benefit the rapid insertion and extraction of lithium ions from the G-NPFMC-S cathode. Intriguingly, this G-NPFMC-S film can be directly used as a binder-free cathode for assembling Li-S battery without adding binders and conductive additives.

Figure 2(a) shows the SEM image of MC at low magnification. It can be seen that ultra-small pores of ~ 15 nm uniformly existed across the whole region of MC nanomaterials. A high-resolution SEM image (Fig. 2(b)) clearly shows the pores that were achieved by chemical etching of the inserted SiO_2 nanoparticles. N_2 adsorption-desorption experiments at 77 K were performed to investigate the porous structures and pore size distribution of MC nanomaterials. As seen in Fig. 2(c), sorption isotherms of N_2 exhibit similar behavior of combinational I/IV type for MC. The pronounced hysteresis loop at P/P_0 above 0.45 and rapid adsorption at high relative pressure are typical characteristics of mesopores [29]. As a result, this MC nanomaterial has achieved a high specific surface area of 921 $m^2 \cdot g^{-1}$. Pore size distribution indicates that an average pore diameter of 15 nm was achieved (inset in Fig. 2(c)), which is consistent with the SEM observations. Figure 2(d) shows the SEM image of NPFMC. It can be seen that the uniform pores were perfectly preserved. The successful doping of N, P and F elements was confirmed by the EDS results (Fig. 2(e)).

The surface compositions and bonding environments were characterized by XPS analyses. Apart from the adsorbed O element, XPS survey spectrum (Fig. S3 in the ESM) of NPFMC shows only N, P, F, C peaks without any other elemental signals. The C 1s core level spectrum (Fig. 2(f)) can be fitted into four components located at 284.9, 285.4, 286.8 and 289.1 eV, representing C-C/C=C, C-N/C=N/C-P, C-F, and O=C-O bonds, respectively [30]. The high-resolution N 1s spectrum can be divided into three peaks (Fig. 2(g)), which represent pyridinic-N (398.3 eV), pyrrolic-N (399.2 eV) and graphitic-N (400.4 eV). Figure 2(h) shows the high-resolution P 2p XPS spectrum, and two main peaks assigned to P-C bond (132.8 eV) and P-O bond (134.3 eV) can be observed.

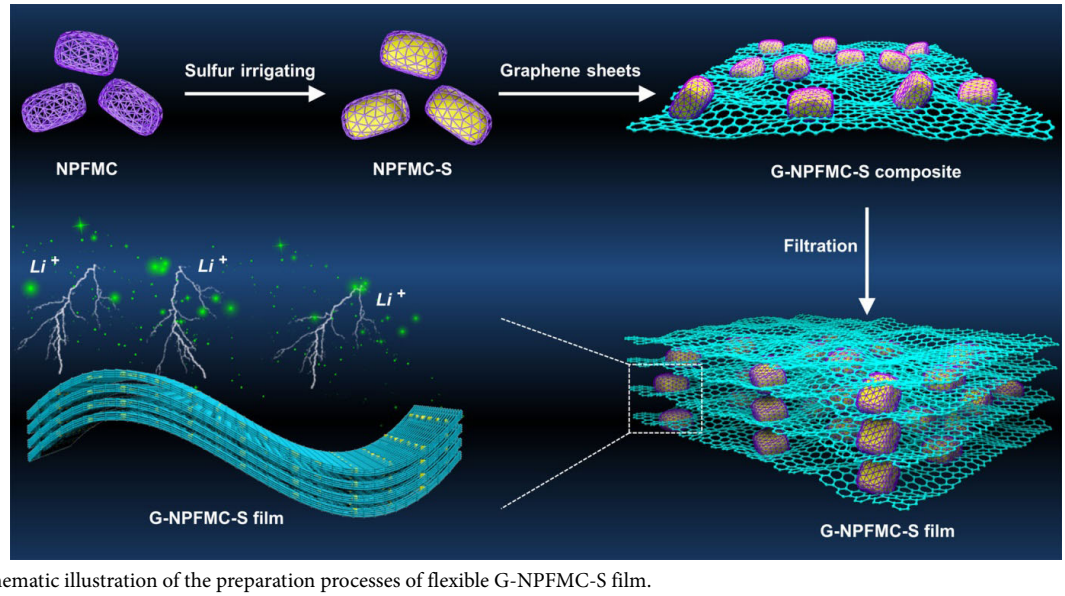

Figure 1 Schematic illustration of the preparation processes of flexible G-NPFMC-S film.

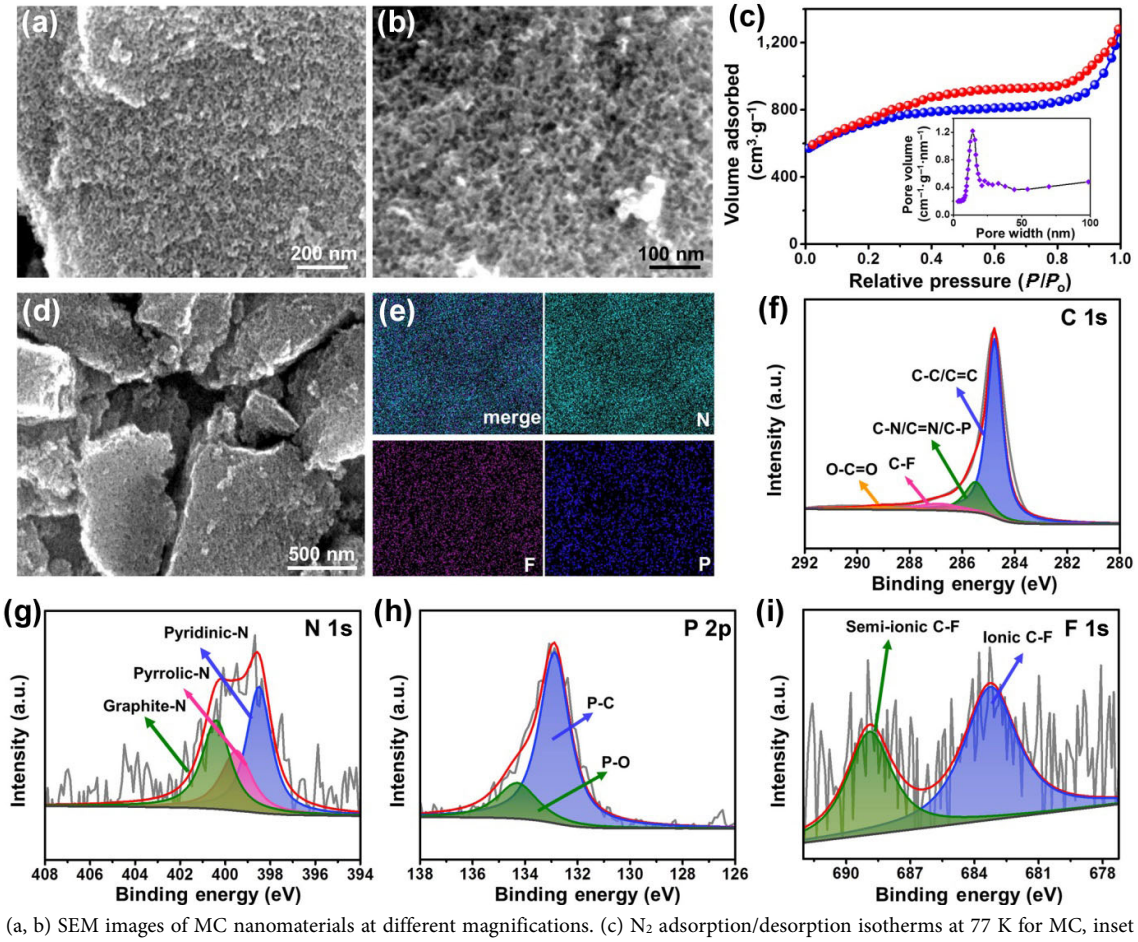

Figure 2 (a, b) SEM images of MC nanomaterials at different magnifications. (c) N_2 adsorption/desorption isotherms at 77 K for MC, inset shows the pore size distribution. (d) SEM image of NPFMC nanomaterial at low magnification and (e) corresponding elemental mapping images of N, P, F elements. High-resolution XPS spectra of (f) C 1s, (g) N 1s, (h) P 2p and (i) F 1s.

Also, high-resolution F 1s spectrum (Fig. 2(i)) shows the characteristic ionic C-F bond (683.2 eV) and semi-ionic C-F bond (688.9 eV) [31–33]. All these XPS detections can demonstrate the successful doping N, P, F atoms on the surface of MC. Furthermore, the introduction of these heteroatoms can effectively enhance the surface/interface polarity of MCs, which will benefit the chemical adsorption of sulfur intermediates during the charge/discharge processes.

Figure 3(a) shows the cross-section of the G-NPFMC-S film. It can be seen that the NPFMC-S nanoparticles were uniformly dispersed together with the graphene sheets. The formed G-NPFMC-S film achieves an excellent porous structure. Meanwhile, a thickness of 50 μm is realized according to the introduction of graphene sheets, which help the formation of film structure. Meanwhile, EDS mappings (Fig. 3(b)) confirm the homogenously dispersed sulfur across the whole region of G-NPFMC-S film. Detailed structural analysis at high resolution shows that graphene layers were coated on the surface of NPFMC-S nanoparticles (Fig. 3(c)), which will undoubtedly act as an interfacial net for physical restriction of the shuttle of LiPS. Correspondingly, the decreased specific surface area (220 $m^2 \cdot g^{-1}$) of G-NPFMC-S can be ascribed to the introduction of sulfur (Fig. S4 in the ESM). Thermogravimetric analysis (TGA) curves show that the sulfur content in this G-NPFMC-S film is about 86 wt.% (Fig. S5 in the ESM). XRD was performed to investigate the composition and crystalline structure evolution of the products. As shown in Fig. 3(d), NPFMC shows a board diffraction peak at about 25.6°, indicating its amorphous carbon nature [34–41]. After impregnating with sulfur, the G-NPFMC-S film shows a series of sharp diffraction peaks corresponding to the orthorhombic sulfur (JCPDS No. 08-0247) [42, 43]. These results are also consistent with the XRD detections of pure sulfur (Fig. 3(d)). Figure 3(e) shows the electrical conductivity of G-NPFMC-S film. It can be seen that the G-NPFMC-S film can substitute a short length of copper wire in the integrated closed loop. This result demonstrates that electrons can rapidly transfer across the whole G-NPFMC-S film, indicating that a good conductive pathway is constructed inside this composite film. Intriguingly, this G-NPFMC-S film is highly flexible and it can be easily bent at a large angle (inset in Fig. 3(e)). Furthermore, the electrical conductivity of G-NPFMC-S film was evaluated by *I*–*V* curve. As seen in Fig. 3(f), the *I*–*V* characteristics of G-NPFMC-S film are precisely linear at the applied voltages from –2.5 to 2.5 V, indicating a good electron transportation capability achieved by this G-NPFMC-S film, which finally reached a promising electrical conductivity of 7,654 $S \cdot m^{-1}$. This excellent conductive property and the favourable porous structures of G-NPFMC-S film can contribute to the rapid insertion and extraction of lithium ions and help the fast transfer of electrons inside the cathode.

To systematically explore the electrochemical behavior of G-NPFMC-S with respect to regulating sulfur chemistry, a columnar Li-S battery was assembled with this free-standing

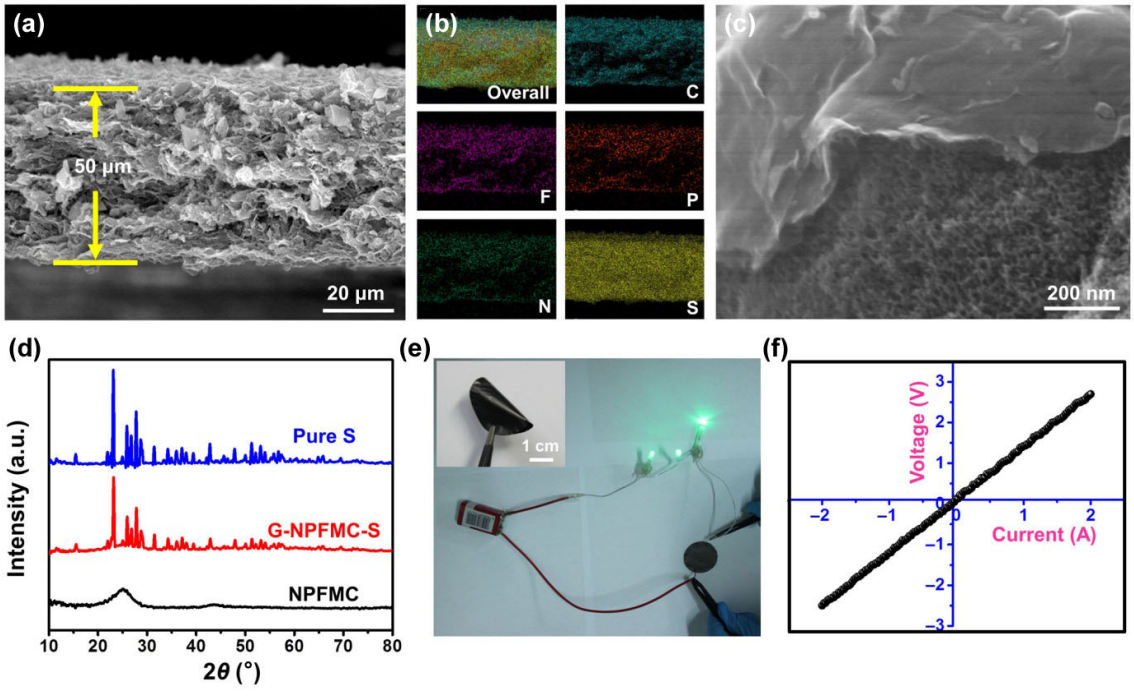

Figure 3 (a) A typical cross-sectional SEM image of G-NPFMC-S film and (b) corresponding elemental mappings of C, F, P, N and S. (c) Enlarged SEM image of the microstructure for G-NPFMC-S. (d) XRD curves of NPFMC, G-NPFMC-S and pure S samples. (e) Optical photograph shows the electrical conductivity of G-NPFMC-S film in an integrated closed loop with G-NPFMC-S substituting a short length of copper wire, inset shows the flexible property of G-NPFMC-S. (f) *I*–*V* curve tested for the G-NPFMC-S film.

G-NPFMC-S as cathode electrode without any addition of polymer binder and conductive additive (Fig. 4(a)). Figure 4(b) depicts the typical CV curves of the batteries at a scan rate of 0.1 mV·s^{-1} for the 1st, 2nd, 3rd and 10th cycles. Two featured cathodic peaks were found during the discharge process. The first peak located at 2.2–2.4 V can be attributed to the formation of long-chain LiPSs, and the second peak at 2.0–2.1 V resulted from the formation of Li_2S_2/Li_2S products [44]. Also, a main anodic peak at about 2.3–2.5 V suggests the oxidation of Li_2S_2/Li_2S to S_8 molecule [45]. The CV curves at the 2nd, 3rd and 10th cycles are nearly overlapped as a result of the good cycling capability achieved by this hierarchical G-NPFMC-S film. Figure 4(c) shows the galvanostatic discharge/charge curves of MC-S, NPFMC-S and G-NPFMC-S cathodes at 0.1 C (1 C = 1,672 mA·g^{-1}). In the discharge curve of G-NPFMC-S cathode, two typical plateaus were observed at 2.32 and 2.10 V, which are attributed to the multistep reduction from sulfur to high order LiPS (L_2S_n, $4 \le n \le 8$), and further to low order LiPS (L_2S_n, $1 \le n \le 4$), respectively [46]. The plateau observed in the charge curve (2.25–2.40 V) is consistent with the anodic peak in the CV curves. The discharge capacities at 0.1 C of Li-S batteries with MC-S, NPFMC-S and G-NPFMC-S cathodes are 642, 892 and 1,356 mAh·g^{-1}, respectively. Here, the superior specific capacity of G-NPFMC-S compared with MC-S and NPFMC-S can be ascribed to the reason that no polymer binder and conductive additive were needed in the G-NPFMC-S cathode. While, for MC-S and NPFMC-S cathodes, the addition of polymer binder and conductive graphite will decrease the utilization efficiency of active sulfur.

Furthermore, the EIS of MC-S, NPFMC-S and G-NPFMC-S cathodes were evaluated to charge the ion-transport capacities, and corresponding Nyquist plots were shown in Fig. 4(d). Here, all the batteries were at fresh state before testing. The overall Nyquist plots are composed of a semicircle and a sloping line in high- and low-frequency regions. G-NPFMC-S cathode shows the smallest depressed semicircle at high frequency, indicating its lowest charge transfer resistance compared with the results of MC-S and NPFMC-S. The EIS fitting results of R_s (bulk resistance), R_{ct} (charge transfer resistance), and Z_W (semi-infinite Warburg diffusion resistance) were conducted based on a proposed equivalent circuit model (Fig. S6 in the ESM). These three kinds of cathodes show similar R_s of ~ 8 Ω. While, G-NPFMC-S cathode shows a R_{ct} value of 35 Ω, which is much smaller than NPFMC-S (52 Ω) and MC-S (60 Ω). Here, the decreased resistance of NPFMC-S compared with MC-S can be ascribed to the reason that the increment of interfacial heteroatoms is beneficial to the formation of a localized donor state close to the Fermi level, and the improvement of the state density of the Fermi surface, further resulting in the enhancement of the conductivity of the NPFMC-S nanomaterial. Also, the further decreased resistance of G-NPFMC-S cathode resulted from the inserting of graphene network, which effectively increased the transfer capability of electrons inside the G-NPFMC-S film.

The rate capabilities of the three cathodes were further investigated at various current densities from 0.1, 0.2, 0.5, 1.0 to 2.0 C. As shown in Fig. 4(e), the corresponding average reversible capacities for the G-NPFMC-S cathode were 1,335, 1,165, 1,026, 934 and 870 mAh·g^{-1}, respectively. Discharge/charge voltage profiles of Li-S batteries with G-NPFMC-S cathode at 0.1, 0.2, 0.5, 1.0 and 2.0 C were shown in Fig. S7 in the ESM. After the high-rate cycling, a high specific discharge capacity of 1,135 mAh·g^{-1} was recovered at 0.1 C. The MC-S and NPFMC-S cathodes show initial specific capacities of 911 and 670 mAh·g^{-1} at 0.1 C, respectively. However, the capacity gaps between these two cathodes and G-NPFMC-S increased with

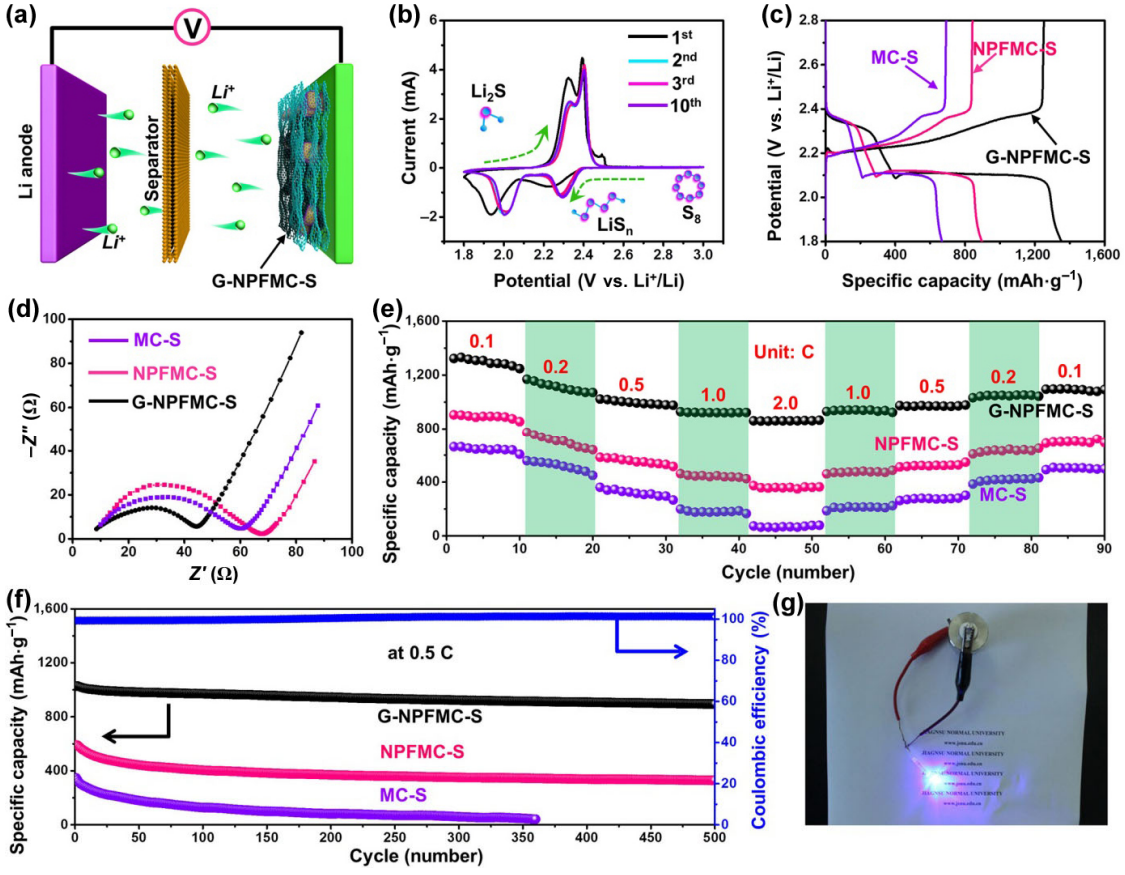

Figure 4 (a) Schematic illustration of the assembled Li-S battery with G-NPFMC-S film as the cathode. (b) CV curves of G-NPFMC-S cathode at a scan rate of 0.1 mV·s^{-1} at the 1st, 2nd, 3rd and 10th cycles. (c) Galvanostatic discharge/charge voltage profiles of Li-S batteries with MC-S, NPFMC-S and G-NPFMC-S cathodes at 0.1 C. (d) Nyquist plots, (e) rate capability and (f) long-term cycling performances for MC-S, NPFMC-S and G-NPFMC-S cathodes. (g) A purple LED was lit up using a column Li-S battery with G-NPFMC-S cathode.

the current density increasing, and only 365 and 72 mAh·g^{-1} were achieved when the current density was increased to 2.0 C. This phenomenon can be ascribed to the reason that polarization occurred in the cathodes of MC-S and NPFMC-S at higher rates, which were greatly decreased in the G-NPFMC-S cathode as graphene networks were introduced throughout the whole film.

Cycling stability tests were carried out to evaluate the lifespan of these electrodes. Here, the columnar Li-S batteries were pre-activated at 0.1 C for five cycles before the electrochemical tests in order to increase the accessibility of electrolyte to sulfur, as that a certain amount of sulfur inside hollow nanocavities or pores can get into contact with the electrolyte and become fully electrochemically active [47]. G-NPFMC-S electrode shows a high initial specific capacity of 1,027 mAh·g^{-1} at 0.5 C (Fig. 4(f)). The discharge capacity was well maintained with a value of 900 mAh·g^{-1} even after 500 cycles. The average Coulombic efficiency and capacity decays per cycle are 99.4% and 0.025%, respectively. In contrast, the NPFMC-S and MC-S electrodes exhibit initial specific capacities of 589 and 368 mAh·g^{-1} at 0.5 C. For MC-S electrode, the capacity quickly decreased, and the cathodic electrode can only be cycled for 360 times. These severe damping of MC-S can be ascribed to the prominent shuttle of LiPS from cathode side to the anode side. Comparatively, the NPFMC-S electrode shows a superior lifespan than MC-S, but worse than G-NPFMC-S. The initial specific capacity (589 mAh·g^{-1}) quickly decreased in the first 100 cycles, and was further gradually declined with the cycling number increasing. Finally, a low capacity of 336 mAh·g^{-1} was maintained after 500 cycles, which shows a capacity decay of 0.086% per cycles. These results are due to the introduction of interfacial heteroatoms and the corresponding enhanced surface polarization, which further benefit the chemical adsorption of LiPS to restrict its shuttle effect. To demonstrate its practical application, Li-S battery assembled with G-NPFMC-S cathode can light up a purple light-emitting diode (LED) easily, as seen in Fig. 4(g).

4 Conclusion

In summary, a rationally designed G-NPFMC-S film with hierarchical structures and pass-through electronic transmission pathways was developed and was further used as a binder-free cathode for Li-S batteries. Highly porous MC matrix that used for the host substrate can ensure high mass loading of active sulfur and simultaneously provide sufficient expansion space for the physicochemical reaction of reactive sulfur during the charge/discharge processes. Multiple heteroatoms doping effect on the surface of MC substrate, including N, P and F, can effectively improve the interfacial polarity of carbon matrix and benefit the chemical constraints for LiPS substances. Meanwhile, graphene sheets were co-dispersed with NPFMC-S nanocomposites and finally formed the G-NPFMC-S film, in which the graphene sheets were connected and a series of

graphene networks were formed. These graphene networks can act as physical skin for restricting the shuttle of LiPS toward the electrolyte and the anode side, further contributing to the excellent cycling stability of G-NPFMC-S film. Benefited from these structural features, a greatly decreased charge transfer resistance and an effectively enhanced redox kinetics of G-NPFMC-S were achieved, including an ultrahigh specific capacity of 1,356 $mAh \cdot g^{-1}$, excellent rate capability and long-term cycling stability up to 500 times with an ultra-small capacity decay of 0.025% per cycle. Compared with the bad rate capabilities and poor cycling performances of NPFMC-S and MC-S cathodes, the promising results of G-NPFMC-S were achieved due to the structural advantages, such as no polymer binder and conductive additive were needed for the preparation of cathode, rich interfacial polarization and physical graphene network provide double protection for the shuttling of LiPS. The created G-NPFMC matrix with a variety of mesoporous structures and excellent ion transfer channels can also be adopted as an ideal host for other electrodes, such as lithium metal batteries. Meanwhile, the synthesis strategy developed in this work also holds great promise for the development of various energy storage and conversion devices.

Acknowledgements

This work was financially supported by the National Natural Science Foundation of China (Nos. 52270006 and 22209063), the Natural Science Foundation of the Jiangsu Higher Education Institutions of China (19KJA460004), the Priority Academic Program Development of Jiangsu Higher Education Institutions, and the Natural Science Foundation of Xuzhou City (KC21283).

Electronic Supplementary Material: Supplementary material (additional optical image, SEM image, XPS results and TGA curve) is available in the online version of this article at https://doi.org/10.26599/NRE.2023.9120049.

Declaration of conflicting interests

The authors declare no conflicting interests regarding the content of this article.

References

[1] Liang, X.; Hart, C.; Pang, Q.; Garsuch, A.; Weiss, T.; Nazar, L. F. A highly efficient polysulfide mediator for lithium-sulfur batteries. *Nat. Commun.* **2015**, *6*, 5682.

[2] Bai, S. Y.; Liu, X. Z.; Zhu, K.; Wu, S. C.; Zhou, H. S. Metal-organic framework-based separator for lithium-sulfur batteries. *Nat. Energy* **2016**, *1*, 16094.

[3] Conder, J.; Bouchet, R.; Trabesinger, S.; Marino, C.; Gubler, L.; Villevieille, C. Direct observation of lithium polysulfides in lithium-sulfur batteries using *operando* X-ray diffraction. *Nat. Energy* **2017**, *2*, 17069.

[4] Zhao, S. Q.; He, Y. J.; Wang, Z. W.; Bo, X. X.; Hao, S. M.; Yuan, Y. F.; Jin, H. L.; Wang, S.; Lin, Z. Q. Advancing performance and unfolding mechanism of lithium and sodium storage in SnO_2 via precision synthesis of monodisperse PEG-ligated nanoparticles. *Adv. Energy Mater.* **2022**, *12*, 2201015.

[5] Zhao, S. Q.; Sewell, C. D.; Liu, R. P.; Jia, S. R.; Wang, Z. W.; He, Y. J.; Yuan, K. J.; Jin, H. L.; Wang, S.; Liu, X. Q. et al. SnO_2 as advanced anode of alkali-ion batteries: Inhibiting Sn coarsening by crafting robust physical barriers, void boundaries, and heterophase interfaces for superior electrochemical reaction reversibility. *Adv. Energy Mater.* **2020**, *10*, 1902657.

[6] Seh, Z. W.; Sun, Y. M.; Zhang, Q. F.; Cui, Y. Designing high-energy lithium-sulfur batteries. *Chem. Soc. Rev.* **2016**, *45*, 5605–5634.

[7] Ye, H. L.; Li, Y. G. Towards practical lean-electrolyte Li-S batteries: Highly solvating electrolytes or sparingly solvating electrolytes? *Nano Res. Energy* **2022**, *1*, e9120012.

[8] Zhou, G. M.; Chen, H.; Cui, Y. Formulating energy density for designing practical lithium-sulfur batteries. *Nat. Energy* **2022**, *7*, 312–319.

[9] Du, Z. Z.; Chen, X. J.; Hu, W.; Chuang, C. H.; Xie, S.; Hu, A. J.; Yan, W. S.; Kong, X. H.; Wu, X. J.; Ji, H. X. et al. Cobalt in nitrogen-doped graphene as single-atom catalyst for high-sulfur content lithium-sulfur batteries. *J. Am. Chem. Soc.* **2019**, *141*, 3977–3985.

[10] Mao, Y. Y.; Li, G. R.; Guo, Y.; Li, Z. P.; Liang, C. D.; Peng, X. S.; Lin, Z. Foldable interpenetrated metal-organic frameworks/carbon nanotubes thin film for lithium-sulfur batteries. *Nat. Commun.* **2017**, *8*, 14628.

[11] Zhao, C. X.; Li, X. Y.; Zhao, M.; Chen, Z. X.; Song, Y. W.; Chen, W. J.; Liu, J. N.; Wang, B.; Zhang, X. Q.; Chen, C. M. et al. Semi-immobilized molecular electrocatalysts for high-performance lithium-sulfur batteries. *J. Am. Chem. Soc.* **2021**, *143*, 19865–19872.

[12] Kim, H.; Lee, J.; Ahn, H.; Kim, O.; Park, M. J. Synthesis of three-dimensionally interconnected sulfur-rich polymers for cathode materials of high-rate lithium-sulfur batteries. *Nat. Commun.* **2015**, *6*, 7278.

[13] Li, G. R.; Lu, F.; Dou, X. Y.; Wang, X.; Luo, D.; Sun, H.; Yu, A. P.; Chen, Z. W. Polysulfide regulation by the zwitterionic barrier toward durable lithium-sulfur batteries. *J. Am. Chem. Soc.* **2020**, *142*, 3583–3592.

[14] Pang, Q.; Liang, X.; Kwok, C. Y.; Nazar, L. F. Advances in lithium-sulfur batteries based on multifunctional cathodes and electrolytes. *Nat. Energy* **2016**, *1*, 16132.

[15] Duan, H. Y.; Li, K.; Xie, M.; Chen, J. M.; Zhou, H. G.; Wu, X. F.; Ning, G. H.; Cooper, A. I.; Li, D. Scalable synthesis of ultrathin polyimide covalent organic framework nanosheets for high-performance lithium-sulfur batteries. *J. Am. Chem. Soc.* **2021**, *143*, 19446–19453.

[16] Zhong, Y.; Chao, D. L.; Deng, S. J.; Zhan, J. Y.; Fang, R. Y.; Xia, Y.; Wang, Y. D.; Wang, X. L.; Xia, X. H.; Tu, J. P. Confining sulfur in integrated composite scaffold with highly porous carbon fibers/vanadium nitride arrays for high-performance lithium-sulfur batteries. *Adv. Funct. Mater.* **2018**, *28*, 1706391.

[17] Li, G. R.; Lei, W.; Luo, D.; Deng, Y. P.; Deng, Z. P.; Wang, D. L.; Yu, A. P.; Chen, Z. W. Stringed "tube on cube" nanohybrids as compact cathode matrix for high-loading and lean-electrolyte lithium-sulfur batteries. *Energy Environ. Sci.* **2018**, *11*, 2372–2381.

[18] Wang, J. L.; Han, W. Q. A review of heteroatom doped materials for advanced lithium-sulfur batteries. *Adv. Funct. Mater.* **2022**, *32*, 2107166.

[19] Hou, T. Z.; Chen, X.; Peng, H. J.; Huang, J. Q.; Li, B. Q.; Zhang, Q.; Li, B. Design principles for heteroatom-doped nanocarbon to achieve strong anchoring of polysulfides for lithium-sulfur batteries. *Small* **2016**, *12*, 3283–3291.

[20] Qiu, Y. C.; Li, W. F.; Zhao, W.; Li, G. Z.; Hou, Y.; Liu, M. N.; Zhou, L. S.; Ye, F. M.; Li, H. F.; Wei, Z. H. et al. High-rate, ultralong cycle-life lithium/sulfur batteries enabled by nitrogen-doped graphene. *Nano Lett.* **2014**, *14*, 4821–4827.

[21] Schuster, J.; He, G.; Mandlmeier, B.; Yim, T.; Lee, K. T.; Bein, T.; Nazar, L. F. Spherical ordered mesoporous carbon nanoparticles with high porosity for lithium-sulfur batteries. *Angew. Chem., Int. Ed.* **2012**, *51*, 3591–3595.

[22] Xie, J.; Li, B. Q.; Peng, H. J.; Song, Y. W.; Zhao, M.; Chen, X.; Zhang, Q.; Huang, J. Q. Implanting atomic cobalt within mesoporous carbon toward highly stable lithium-sulfur batteries. *Adv. Mater.* **2019**, *31*, 1903813.

[23] Peng, H. J.; Huang, J. Q.; Cheng, X. B.; Zhang, Q. Review on high-loading and high-energy lithium-sulfur batteries. *Adv. Energy Mater.* **2017**, *7*, 1700260.

[24] Hu, Y.; Chen, W.; Lei, T. Y.; Jiao, Y.; Huang, J. W.; Hu, A. J.; Gong, C. H.; Yan, C. Y.; Wang, X. F.; Xiong, J. Strategies toward high-loading lithium-sulfur battery. *Adv. Energy Mater*. **2020**, *10*, 2000082.
[25] Wang, T.; Zhang, Q. S.; Zhong, J.; Chen, M. X.; Deng, H. L.; Cao, J. H.; Wang, L.; Peng, L. L.; Zhu, J.; Lu, B. G. 3D holey graphene/polyacrylonitrile sulfur composite architecture for high loading lithium sulfur batteries. *Adv. Energy Mater*. **2021**, *11*, 2100448.
[26] Manthiram, A.; Fu, Y. Z.; Su, Y. S. Challenges and prospects of lithium-sulfur batteries. *Acc. Chem. Res*. **2013**, *46*, 1125–1134.
[27] Yan, Y.; Zhang, P.; Qu, Z. H.; Tong, M. M.; Zhao, S.; Li, Z. W.; Liu, M. K.; Lin, Z. Q. Carbon/sulfur aerogel with adequate mesoporous channels as robust polysulfide confinement matrix for highly stable lithium-sulfur battery. *Nano Lett*. **2020**, *20*, 7662–7669.
[28] Liu, Y. Q.; Yan, Y.; Li, K.; Yu, Y.; Wang, Q. H.; Liu, M. K. A high-areal-capacity lithium-sulfur cathode achieved by a boron-doped carbon-sulfur aerogel with consecutive core-shell structures. *Chem. Commun*. **2019**, *55*, 1084–1087.
[29] Qi, D. F.; Lv, F.; Wei, T. R.; Jin, M. M.; Meng, G.; Zhang, S. S.; Liu, Q.; Liu, W. X.; Ma, D.; Hamdy, M. S. et al. High-efficiency electrocatalytic NO reduction to NH_3 by nanoporous VN. *Nano Res. Energy* **2022**, *1*, e9120022.
[30] Zheng, Y.; Ni, X. P.; Li, K. M.; Yu, X. H.; Song, H.; Chen, S.; Khan, N. A.; Wang, D.; Zhang, C. Multi-heteroatom-doped hollow carbon nanocages from ZIF-8@CTP nanocomposites as high-performance anodes for sodium-ion batteries. *Compos. Commun*. **2022**, *32*, 101116.
[31] Liu, Y.; Li, Q. Y.; Guo, X.; Kong, X. D.; Ke, J. W.; Chi, M. F.; Li, Q. X.; Geng, Z. G.; Zeng, J. A highly efficient metal-free electrocatalyst of f-doped porous carbon toward N_2 electroreduction. *Adv. Mater*. **2020**, *32*, 1907690.
[32] Huang, S. Z.; Li, Y.; Feng, Y. Y.; An, H. R.; Long, P.; Qin, C. Q.; Feng, W. Nitrogen and fluorine co-doped graphene as a high-performance anode material for lithium-ion batteries. *J. Mater. Chem. A* **2015**, *3*, 23095–23105.
[33] Guo, X.; Wang, C. D.; Wang, W. J.; Zhou, Q.; Xu, W. J.; Zhang, P. J.; Wei, S. Q.; Cao, Y. Y.; Zhu, K. F.; Liu, Z. F. et al. Vacancy manipulating of molybdenum carbide MXenes to enhance Faraday reaction for high performance lithium-ion batteries. *Nano Res. Energy* **2022**, *1*, e9120026.
[34] Li, G. X.; Sun, J. H.; Hou, W. P.; Jiang, S. D.; Huang, Y.; Geng, J. X. Three-dimensional porous carbon composites containing high sulfur nanoparticle content for high-performance lithium-sulfur batteries. *Nat. Commun*. **2016**, *7*, 10601.
[35] Xue, W. D.; Zhou, Q. X.; Cui, X.; Jia, S. R.; Zhang, J. W.; Lin, Z. Q. Metal-organic frameworks-derived heteroatom-doped carbon electrocatalysts for oxygen reduction reaction. *Nano Energy* **2021**, *86*, 106073.
[36] Zhang, J. W.; Sewell, C. D.; Huang, H. W.; Lin, Z. Q. Closing the anthropogenic chemical carbon cycle toward a sustainable future via CO_2 valorization. *Adv. Energy Mater*. **2021**, *11*, 2102767.
[37] Cui, X.; Gao, L. K.; Lei, S.; Liang, S.; Zhang, J. W.; Sewell, C. D.; Xue, W. D.; Liu, Q.; Lin, Z. Q.; Yang, Y. K. Simultaneously crafting single-atomic fe sites and graphitic layer-wrapped Fe_3C nanoparticles encapsulated within mesoporous carbon tubes for oxygen reduction. *Adv. Funct. Mater*. **2021**, *31*, 2009197.
[38] Ma, D. T.; Li, Y. L.; Mi, H. W.; Luo, S.; Zhang, P. X.; Lin, Z. Q.; Li, J. Q.; Zhang, H. Robust SnO_{2-x} nanoparticle-impregnated carbon nanofibers with outstanding electrochemical performance for advanced sodium-ion batteries. *Angew. Chem., Int. Ed*. **2018**, *57*, 8901–8905.
[39] Guo, F. J.; Zhang, M. Y.; Yi, S. C.; Li, X. X.; Xin, R.; Yang, M.; Liu, B.; Chen, H. B.; Li, H. M.; Liu, Y. J. Metal-coordinated porous polydopamine nanospheres derived Fe_3N-FeCo encapsulated N-doped carbon as a highly efficient electrocatalyst for oxygen reduction reaction. *Nano Res. Energy* **2022**, *1*, e9120027.
[40] Xie, F. R.; Zhao, S. Q.; Bo, X. X.; Li, G. H.; Fei, J. M.; Ahmed, E. A. M. A.; Zhang, Q. C.; Jin, H. L.; Wang, S.; Lin, Z. Q. A robust solvothermal-driven solid-to-solid transition route from micron SnC_2O_4 to tartaric acid-capped nano-SnO_2 anchored on graphene for superior lithium and sodium storage. *J. Mater. Chem. A*, in press, DOI: 10.1039/D2TA07435D.
[41] Zhao, S. Q.; Wang, Z. W.; He, Y. J.; Jiang, H. R.; Harn, Y. W.; Liu, X. Q.; Su, C. L.; Jin, H. L.; Li, Y.; Wang, S. et al. A robust route to $Co_2(OH)_2CO_3$ ultrathin nanosheets with superior lithium storage capability templated by aspartic acid-functionalized graphene oxide. *Adv. Energy Mater*. **2019**, *9*, 1901093.
[42] Dörfler, S.; Strubel, P.; Jaumann, T.; Troschke, E.; Hippauf, F.; Kensy, C.; Schökel, A.; Althues, H.; Giebeler, L.; Oswald, S. et al. On the mechanistic role of nitrogen-doped carbon cathodes in lithium-sulfur batteries with low electrolyte weight portion. *Nano Energy* **2018**, *54*, 116–128.
[43] Li, M.; Zhang, Y. N.; Bai, Z. Y.; Liu, W. W.; Liu, T. C.; Gim, J.; Jiang, G. P.; Yuan, Y. F.; Luo, D.; Feng, K. et al. A lithium-sulfur battery using a 2D current collector architecture with a large-sized sulfur host operated under high areal loading and low E/S ratio. *Adv. Mater*. **2018**, *30*, 1804271.
[44] Tan, J. C.; Li, D.; Liu, Y. Q.; Zhang, P.; Qu, Z. H.; Yan, Y.; Hu, H.; Cheng, H. Y.; Zhang, J. X.; Dong, M. Y. et al. A self-supported 3D aerogel network lithium-sulfur battery cathode: Sulfur spheres wrapped with phosphorus doped graphene and bridged with carbon nanofibers. *J. Mater. Chem. A* **2020**, *8*, 7980–7990.
[45] Zhao, S.; Kang, Y. J.; Liu, M. J.; Wen, B. H.; Fang, Q.; Tang, Y. Y.; He, S. C.; Ma, X.; Liu, M. K.; Yan, Y. Modulating the electronic structure of nanomaterials to enhance polysulfides confinement for advanced lithium-sulfur batteries. *J. Mater. Chem. A* **2021**, *9*, 18927–18946.
[46] Zhang, Q.; Huang, Q. H.; Hao, S. M.; Deng, S. Y.; He, Q. M.; Lin, Z. Q.; Yang, Y. K. Polymers in lithium-sulfur batteries. *Adv. Sci*. **2022**, *9*, 2103798.
[47] Li, Z. L.; Xiao, Z. B.; Wang, S. Q.; Cheng, Z. B.; Li, P. Y.; Wang, R. H. Engineered interfusion of hollow nitrogen-doped carbon nanospheres for improving electrochemical behavior and energy density of lithium-sulfur batteries. *Adv. Funct. Mater*. **2019**, *29*, 1902322.

Haotian Liu received a Bachelor degree of Science degree in Applied Chemistry from South China Agricultural University in 2020. Now, he is a master student in the Laboratory of Quantum Information, Measurement and Control of Sun Yat-Sen University. His main research directions are focusing on quantum multi-body physics based on ultracold Fermi gases, atomic cooling and trapping, and low-dimensional cold atomic physics.

Yan Yan is an associate professor in School of Chemistry and Materials Science at Jiangsu Normal University. She earned her BS degree in Materials Chemistry at Henan University, and later received her PhD in Inorganic Chemistry from Sun Yat-Sen University in 2014. She studied at the Georgia Institute of Technology as a visiting scholar from 2019–2020. Her research interests focus on nanocarbon materials, advanced energy storage/conversion, lithium–sulfur batteries, and catalysis.

Xinming Nie is a senior experimenter in the School of Physics and Electronic Engineering of Jiangsu Normal University. He received a bachelor's degree from Huaiyin Institute of Technology in Jiangsu Province, a master's degree from Guangdong University of Technology, and now is a doctoral candidate from China University of Mining and Technology. His research interests focus on high safety and high performance lithium ion, zinc ion batteries and high energy density gas batteries.

Xin Ma is a professor in School of Chemistry and Materials Science, Nanjing University of Information Science and Technology. He earned his BS degree in Physics Electronics at Zhejiang University, and he received his Master degree in Physics Electronics and later his PhD in Electrical Engineering at Institute of Electronics, Chinese Academy of Sciences in 2000. He studied at Tsinghua University as a post doc. from 2000–2003. Then he worked in research labs in industry until return to Jiangsu Normal University. His research interests focus on anode material and high energy density solid state Li-ion battery.

Mingkai Liu received his BS degree from the School of Chemistry and Chemical Engineering, Henan University in 2008, and then received his M.S. degree in Chemical Engineering from Guangdong University of Technology and Sun Yat-Sen University in 2011, and PhD degree in Macromolecular Science from Fudan University in 2014. He joined Younan Xia's group as a postdoc in Georgia Institute of Technology from 2018–2020. Now, he is an associate professor at Jiangsu Normal University. His research interests include the development of functional nanomaterials for applications in catalysis, energy storage/conversion and environmental science.